TransformerFusion: Monocular RGB Scene Reconstruction using Transformers

Aljaž Božič [1]   Pablo Palafox [1]   Justus Thies [1,2]   Angela Dai [1]   Matthias Nießner [1]

[1]Technical University of Munich
[2]Max Planck Institute for Intelligent Systems, Tübingen, Germany
aljazbozic.github.io/transformerfusion

Abstract

We introduce TransformerFusion, a transformer-based 3D scene reconstruction approach. From an input monocular RGB video, the video frames are processed by a transformer network that fuses the observations into a volumetric feature grid representing the scene; this feature grid is then decoded into an implicit 3D scene representation. Key to our approach is the transformer architecture that enables the network to learn to attend to the most relevant image frames for each 3D location in the scene, supervised only by the scene reconstruction task. Features are fused in a coarse-to-fine fashion, storing fine-level features only where needed, requiring lower memory storage and enabling fusion at interactive rates. The feature grid is then decoded to a higher-resolution scene reconstruction, using an MLP-based surface occupancy prediction from interpolated coarse-to-fine 3D features. Our approach results in an accurate surface reconstruction, outperforming state-of-the-art multi-view stereo depth estimation methods, fully-convolutional 3D reconstruction approaches, and approaches using LSTM- or GRU-based recurrent networks for video sequence fusion.

1   Introduction

Monocular 3D reconstruction is a core task in 3D computer vision, aiming to reconstruct a complete and accurate 3D geometry of an object or an environment from only 2D observations captured by an RGB camera. A geometric understanding is key to applications such as robotic or autonomous vehicle navigation or interaction, as well as model creation and scene editing for augmented and virtual reality. In addition, geometric scene reconstructions form the basis for 3D scene understanding, supporting tasks such as 3D object detection, semantic, and instance segmentation [34, 35, 36, 29, 7, 43, 15, 16].

While state-of-the-art SLAM systems [3, 41] achieve robust and scale-accurate camera tracking leveraging both visual and inertial measurements, dense and complete 3D reconstruction of large-scale environments from monocular video remains a very challenging problem – particularly for interactive settings. Simultaneously, notable progress has been made on multi-view depth estimation, estimating depth from pairs of images by averaging features extracted from the images in a feature cost volume [42, 17, 19, 38, 13]. Unfortunately, averaging features across a full video sequence can lead to equal-weight treatment of each individual frame, despite some frames possibly containing less information in various regions (e.g., from motion blur, rolling shutter artifacts, very glancing or partial views of objects), making high-fidelity scene reconstruction challenging.

Inspired by the recent advances in natural language processing (NLP) that leverage transformer-based models for sequence to sequence modelling [40, 11, 2], we propose a transformer-based method that fuses a sequence of RGB input frames into a 3D representation of a scene at interactive rates. Key to
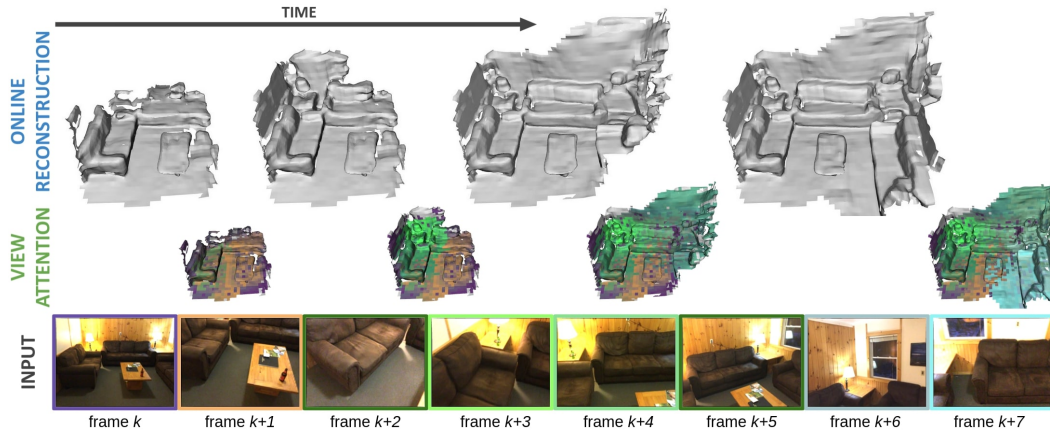
Figure 1: TransformerFusion is an online scene reconstruction method that takes a monocular RGB video as input. The features extracted from each observed image are fused incrementally with a transformer architecture. This fusion approach learns to attend to the most relevant image frames for each 3D location (see view attention color maps of the most relevant frame) achieving state-of-the-art reconstruction results.

our approach is a learned feature fusion of the video frames using a transformer-based architecture, which learns to attend to the most informative image features to reconstruct a local 3D region of the scene. A new observed RGB frame is encoded into a 2D feature map, and unprojected into a 3D volume, where our transformer learns a fused 3D feature for each location in the 3D volume from the image view features. This enables extraction of the most informative view features for each location in the 3D scene. The 3D features are fused in coarse-to-fine fashion, providing both improved reconstruction performance as well as interactive runtime. These features are then decoded into high-resolution scene geometry with an MLP-based surface occupancy prediction.

In summary, our main contributions to achieve robust and accurate scene reconstructions are:

- Learned multi-view feature fusion in the temporal domain using a transformer network that attends to only the most informative features of the image views for reconstructing each location in a scene.
- A coarse-to-fine hierarchy of our transformer-based feature fusion that enables an online reconstruction approach running at interactive frame-rates.

2 Related Work

Multi-view depth estimation. Estimating depth from multi-view image observations has been long-studied in computer vision. COLMAP [37] introduced a patch matching based approach which achieves impressive accuracy and remains established as one of the most popular methods for multi-view stereo. While COLMAP offers robust depth estimation for distinctive features in images, the patch matching struggles to densely reconstruct areas without many distinctive color features, such as floor and walls. Recently, learning-based approaches that build data-driven priors from large-scale datasets have improved depth estimation in these challenging scenarios. Some proposed methods rely only on a 2D network with multiple images concatenated as input [42]. Several recent approaches instead build a shared 3D feature cost volume in reference camera space using feature averaging [13, 17, 19, 25, 26]. These approaches estimate the reference frame's depth within a local window of frames, but some also propagate information from previously estimated depth maps by using probabilistic filtering [25], a Gaussian process [17], or an LSTM bottleneck layer [13]. Such multi-view depth estimation approaches predict single-view depth maps, which must be fused together to construct a geometric 3D representation of the observed scene.

3D reconstruction from monocular RGB input. Multi-view depth estimation approaches can be combined with depth fusion approaches, such as volumetric fusion [6], to obtain a volumetric

2

reconstruction of the observed scene. MonoFusion [33] is one of the first methods using depth estimate from a real-time variant of PatchMatch stereo [1]. However, fusing noisy depth estimates causes artifacts in the 3D reconstruction, which lead to the development of recent approaches that directly predict the 3D surface reconstruction instead of per-frame depth estimates. One of the first approaches to predict 3D surface occupancy from two input RGB images is SurfaceNet [20], which converts volumetrically averaged colors into 3D surface occupancies using a 3D convolutional network. Atlas [28] extends this approach to a multi-view setting, while also leveraging learned features instead of colors. Recently, NeuralRecon [39] proposed a real-time 3D reconstruction framework, adding GRU units distributed in 3D to fuse reconstructions from different local windows of frames. Our approach also fuses together learned features from RGB frame input in an online fashion, but our transformer-based multi-view feature fusion enables relying only on the most informative features from the observed frames for a particular spatial location in the reconstructed scene, producing more accurate 3D reconstructions.

Transformers in computer vision.   The transformer architecture [40] has achieved profound impact in many computer vision tasks in addition to its natural language processing origins. For a detailed survey, we refer the reader to [22]. In computer vision, transformers have been leveraged successfully for tasks such as object detection [4], video classification [44], image classification [12], image generation [30], and human reconstruction [45]. In this work, we propose transformer-based feature fusion for 3D scene reconstruction from a monocular video. Given a sequence of observed RGB frames, our approach learns to attend to the most informative features from each image to predict a dense occupancy field.

3   End-to-end 3D Reconstruction using Transformers

Given a set of N RGB images $I_i \in \mathbb{R}^{W \times H \times 3}$ of a scene with corresponding camera intrinsic parameters $\mathbf{K}_i \in \mathbb{R}^{3 \times 3}$ and extrinsic poses $\mathbf{P}_i \in \mathbb{R}^{4 \times 4}$, our method reconstructs the scene geometry by predicting occupancy values $o \in [0, 1]$ for every 3D point in the scene. Fig. 2 shows an overview of our approach. Each input image I_i is processed by a 2D convolutional encoder Θ, extracting coarse and fine image features (Φ_i^c and Φ_i^f, respectively):

$$\Theta : I_i \in \mathbb{R}^{W \times H \times 3} \mapsto (\Phi_i^c, \Phi_i^f)$$

From these 2D image features, we construct a 3D feature grid in world space. To this end, we regularly sample grid points in 3D at a coarse resolution of every $v_c = 30$ cm and a fine resolution of $v_f = 10$ cm. For these coarse and fine sample points, we query corresponding 2D features in all N images and predict fused coarse ψ^c and fine 3D features ψ^f using transformer networks [40]:

$$\mathcal{T}_c : (\Phi_1^c, \ldots, \Phi_N^c) \mapsto (\psi^c, w^c)$$
$$\mathcal{T}_f : (\Phi_1^f, \ldots, \Phi_N^f) \mapsto (\psi^f, w^f)$$

Note that we also store the intermediate attention weights w^c and w^f of the first transformer layers for efficient view selection, which is explained in Sec. 3.4.

To further improve the features in the 3D spatial domain, we apply 3D convolutional networks $\mathcal{C}_c$ and $\mathcal{C}_f$, at the coarse and fine level, respectively:

$$\mathcal{C}_c : \{\psi^c\}_{C \times C \times C} \mapsto \{\tilde{\psi}^c\}_{C \times C \times C}$$
$$\mathcal{C}_f : \{(\tilde{\psi}^c, \psi^f)\}_{F \times F \times F} \mapsto \{\tilde{\psi}^f\}_{F \times F \times F}$$

Finally, to predict the scene geometry occupancy for a point $\mathbf{p} \in \mathbb{R}^3$, the coarse $\tilde{\psi}_c$ and fine features $\tilde{\psi}_f$ are trilinearly interpolated and a multi-layer perceptron $\mathcal{S}$ maps these features to occupancies:

$$\mathcal{S} : (\tilde{\psi}^c, \tilde{\psi}^f) \mapsto o \in [0, 1]$$

This extraction of surface occupancies is inspired by convolutional occupancy networks [32] and IFNets [5]. From this occupancy field we extract a surface mesh with Marching cubes [27]. Note that in addition to surface occupancy, we also predict occupancy masks for near-surface locations at the coarse and fine levels. These masks are used for coarse-to-fine surface filtering (see Sec. 3.2), which

improves reconstruction performance with a focus on the surface geometry prediction and enables interactive runtime.

We train our approach in end-to-end fashion by supervising the surface occupancy predictions using the following loss:

$$\mathcal{L} = \mathcal{L}_c + \mathcal{L}_f + \mathcal{L}_o,$$

where $\mathcal{L}_c$ and $\mathcal{L}_f$ denote binary cross-entropy (BCE) losses on occupancy mask predictions for near-surface locations at the coarse and fine levels, respectively (see Sec. 3.2), and $\mathcal{L}_o$ denotes a BCE loss for surface occupancy prediction (see Sec. 3.3).
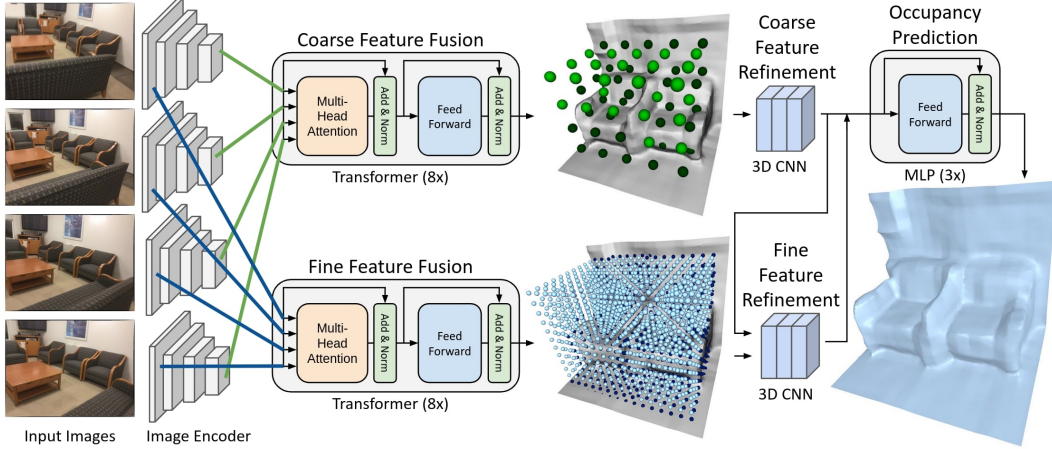

Figure 2: Method overview: given multiple input images, we compute coarse and fine level features. Using a transformer architecture, we separately fuse these coarse and fine features in a voxel grid. To improve the spatial features, we use a refinement network for both the coarse and the fine features. From these feature grids, we extract an occupancy field using a lightweight MLP.

3.1 Learning Temporal Feature Fusion via Transformers

For a spatial location $\mathbf{p} \in \mathbb{R}^3$ in the scene reconstruction, we learn to fuse coarse ψ^c and fine level features ψ^f from the N coarse and fine feature images (Φ_i^c and Φ_i^f, respectively), which are extracted by the 2D encoder Θ. Specifically, we train two instances of a transformer model, one for fusing coarse-level features ψ^c and one for fusing fine-level features ψ^f. Both transformers $\mathcal{T}_c$ and $\mathcal{T}_f$ share the same architecture. Thus, for simplicity, we omit the coarse and fine notation in the following.

Our transformer model $\mathcal{T}$ is independently applied to each sample point in world space. For a point $\mathbf{p}$, the transformer network takes a series of 2D features ϕ_i as input that are bilinearly sampled from the feature maps Φ_i at the corresponding projective image location. The projective image location is computed via a full-perspective projection $\Pi_i(\mathbf{p}) = \pi(\mathbf{K}_i(\mathbf{R}_i\mathbf{p} + \mathbf{t}_i))$, assuming known camera intrinsics $\mathbf{K}_i$ and extrinsics $\mathbf{P}_i = (\mathbf{R}_i, \mathbf{t}_i)$. To inform the transformer about invalid features (i.e., a sample point is projected outside an image), we also provide the pixel validity $v_i \in \{0, 1\}$ as input. In addition to these 2D features ϕ_i, we concatenate the projected depth $d_i = (\mathbf{R}_i\mathbf{p} + \mathbf{t}_i)_z$, and the viewing ray $\mathbf{r_i} = (\mathbf{p} - \mathbf{c}_i)/||\mathbf{p} - \mathbf{c}_i||_2$ to the input ($\mathbf{c}_i \in \mathbb{R}^3$ denoting the camera center of view i). These input features are converted to an embedding vector $\theta_i \in \mathbb{R}^D$ using a linear layer $\theta_i = \mathbf{FCN}(\phi_i, d_i, v_i, \mathbf{r_i})$, before feeding it into the transformer network that then predicts a fused feature $\psi \in \mathbb{R}^D$:

$$\mathcal{T} : (\theta_1, \ldots, \theta_N) \mapsto (\psi, w)$$

As described above, w denotes the attention values of the initial attention layer, which are used for view selection to speed-up fusion (see Sec. 3.4).

Transformer architecture. We followed [12] when designing the transformer architecture $\mathcal{T}$. It consists of 8 modules of feed-forward and attention layers, using multi-head attention with 4 attention heads and embedding dimension $D = 256$. Feed-forward layers process the temporal inputs independently, and contain ReLU activation, linear layers with residual connection, and layer norm.

The model returns both fused feature $\psi \in \mathbb{R}^D$ and attention weights $w \in \mathbb{R}^N$ over all temporal inputs from the initial attention layer that are later used for selecting which views to maintain over longer sequences of input image views.

3.2 Spatial Feature Refinement

While the transformer network fuses 2D observations in the temporal domain, we additionally imbue explicit spatial reasoning by applying a 3D CNN to spatially refine the fused features $\{\psi^c\}_{C \times C \times C}$ and $\{\psi^f\}_{F \times F \times F}$ that are computed by the transformers $\mathcal{T}_c$ and $\mathcal{T}_f$ on the coarse and fine grid, respectively. The coarse features $\{\psi^c\}_{C \times C \times C}$ are refined by a 3D CNN $\mathcal{C}_c$ consisting of 3 residual blocks that maintain the same spatial resolution and produce refined features $\{\tilde{\psi}^c\}_{C \times C \times C}$. These features are upsampled to a fine grid resolution using nearest-neighbor upsampling, and concatenated with fused features at fine level $\{\psi^f\}_{F \times F \times F}$. A fine-level 3D CNN $\mathcal{C}_f$ is then applied to the concatenated features, resulting in refined fine features $\{\tilde{\psi}^f\}_{F \times F \times F}$. Both, coarse $\tilde{\psi}^c$ and fine features $\tilde{\psi}^f$ are used for surface occupancy prediction.

Coarse-to-fine surface filtering. The refined features are also used to predict occupancy masks for near-surface locations at both coarse and fine levels, thus, filtering out free-space regions and sparsifying the volume, such that the higher-resolution and computationally expensive fine-scale surface extraction is performed only in regions close to the surface. To achieve this, additional 3D CNN layers $\mathcal{M}_c$ and $\mathcal{M}_f$ are applied to the refined features, outputting a near-surface mask $m^c, m^f \in [0, 1]$ for every grid point:

$$\mathcal{M}_c : \{\tilde{\psi}^c\}_{C \times C \times C} \mapsto \{m^c\}_{C \times C \times C}$$
$$\mathcal{M}_f : \{\tilde{\psi}^f\}_{F \times F \times F} \mapsto \{m^f\}_{F \times F \times F}$$

Only spatial regions where both m^c and m^f are larger than 0.5, i.e., close to the surface, are processed further to compute the final surface reconstruction; other regions are determined to be free space. This improves the overall reconstruction performance by focusing the capacity of the surface prediction network to close-to-the-surface regions and enables a significant runtime speed-up.

Intermediate supervision of near-surface masks m^c and m^f is employed using masks m_{gt}^c and m_{gt}^f generated from the ground truth scene reconstruction, denoting the grid point as near-surface if there exists ground truth surface in the radius of v_c or v_f from the point. Binary cross entropy losses $\mathcal{L}_c = \text{BCE}(m^c, m_{\text{gt}}^c)$ and $\mathcal{L}_f = \text{BCE}(m^f, m_{\text{gt}}^f)$ are applied.

3.3 Surface Occupancy Prediction

The final surface reconstruction is predicted by decoding the coarse and fine feature grids to occupancy values $o \in [0, 1]$, with values $o \geq 0.5$ representing occupied points and values $o < 0.5$ representing free-space points. For a point $\mathbf{p} \in \mathbb{R}^3$, we compute its feature representation by trilinearly interpolating coarse and fine grid features:

$$\psi_{\mathbf{p}}^c = \text{Trilinear}(\mathbf{p}, \{\tilde{\psi}^c\}_{C \times C \times C})$$
$$\psi_{\mathbf{p}}^f = \text{Trilinear}(\mathbf{p}, \{\tilde{\psi}^f\}_{F \times F \times F})$$

We concatenate the interpolated features and predict the point's occupancy as $o = \mathcal{S}(\psi_{\mathbf{p}}^c, \psi_{\mathbf{p}}^f)$, where $\mathcal{S}$ is a multi-layer perceptron (MLP) with 3 modules of feed-forward layers, containing ReLU activation, linear layer with residual connection, and layer norm.

Surface occupancy supervision. We train on $1.5 \times 1.5 \times 1.5$ m volumetric chunks of scenes for training efficiency. To supervise the surface occupancy loss, 1k points are sampled inside the chunk, with 80% of samples drawn from a truncation region at most 10 cm from the surface, and 20% sampled uniformly inside the chunk. Ground truth occupancy values o_{gt} are computed using the ScanNet RGB-D reconstructions [8]. For uniform samples it is straightforward to generate unoccupied point samples by sampling points in free space in front of the visible surface, but it is unknown whether a point sample is occupied when it lies behind seen surfaces. In order to prevent artifacts behind walls, we follow the data processing applied in [28] and additionally label point samples as occupied, if they are sampled in areas where an entire vertical column of voxels is occluded in the scene. A binary cross entropy loss $\mathcal{L}_o = \text{BCE}(o, o_{\text{gt}})$ is then applied to the occupancy predictions o.

3.4 View Selection for Online Scene Reconstruction

We aim to consider all N frames as input to our transformer for each 3D location in a scene; however, this becomes extremely computationally expensive with long videos or large-scale scenes, which prohibits online scene reconstruction. Instead, we proceed with the reconstruction incrementally, processing every video frame one-by-one, while keeping only a small number $K = 16$ of measurements for every 3D point. We visualize this online approach in Fig. 1.

During training, for efficiency, we use only K_t random images for each training volume. At test time, we leverage the attention weights w^c and w^f of the initial transformer layers to determine which views to keep in the set of K measurements. Specifically, for a new RGB frame, we extract its 2D features, and run feature fusion for every coarse and fine grid point inside the camera frustum. This returns the fused feature and also the attention weights over all currently accumulated input measurements. Whenever the maximum number of K measurements is reached, a selection is made by dropping out a measurement with lowest attention weight before adding new measurements in the latest frame. This guarantees a low number of input measurements, speeding up fusion processing times considerably. Furthermore, by using coarse-to-fine filtering, described in Sec. 3.2, we can further accelerate fusion by only considering higher resolution points in the area near the estimated surface. Together with incremental processing that results in high performance benefits, our approach performs per-frame feature fusion at about 7 FPS despite an unoptimized implementation.

3.5 Training Scheme

Our approach has been implemented using the PyTorch library [31]. The architecture details of the used networks are specified in the supplemental document. To train our approach we use ScanNet dataset [8], an RGB-D dataset of indoor apartments. We follow the established train-val-test split. For training, we randomly sample $1.5 \times 1.5 \times 1.5$ m volume chunks of the train scenes, sampling less chunks in free space and more samples in areas with non-structural objects, i.e. not only consisting of floor or walls. This results in ≈ 165k training chunks. For each chunk, we randomly sample $K_t = 8$ RGB images among all frames that include the chunk in their camera frustums.

The 2D convolutional encoder Θ for image feature extraction is implemented as a ResNet-18 [14] network, pre-trained on ImageNet [24]. During training, a batch size of 4 chunks is used with an Adam [23] optimizer with $\beta_1 = 0.9$, $\beta_2 = 0.999$, $\epsilon = 10^{-8}$ and weight regularization of 10^{-4}. We use a learning rate of 10^{-4} with 5k warm-up steps at initialization, and square root learning rate decay afterwards. When computing the losses of coarse and fine surface filtering predictions, a higher weight of 2.0 is applied to near-surface voxels, to increase recall and improve overall robustness. Training takes about 30 hours using an Intel Xeon 6242R Processor and an Nvidia RTX 3090 GPU.

4 Experiments

Metrics. To evaluate our monocular scene reconstruction, we use several measures of reconstruction performance. We evaluate geometric accuracy and completion, with accuracy measuring the average point-to-point error from predicted to ground truth vertices, completion measuring the error in the opposite direction, and chamfer as the average of accuracy and completion. To account for possibly different mesh resolutions among methods, we uniformly sample 200k points over mesh faces of every reconstructed mesh. Additionally, we threshold these point-to-point errors and compute precision and recall by computing the ratio of point-to-point matches within distance ≤ 5cm. Since it is easy to maximize either precision (by predicting only a few but accurate points) or recall (by over-completing reconstructions with noisy surface), we found the most reliable metric to be F-score, determined by both precision and recall.

Our ground truth reconstructions are obtained by automated 3D reconstruction [9] from RGB-D videos of real-world environments and, thus, they are often incomplete due to unobserved and occluded regions in the scene. To avoid penalizing methods for reconstructing a more complete scene w.r.t. the available ground truth, we apply an additional occlusion mask at evaluation.

As most state of the art, particularly for depth estimation, rely on a pre-sampled set of keyframes (based on sufficient translation or rotation difference between camera poses), we evaluate all approaches based on sequences of sampled keyframes, using the keyframe selection of [13].

Table 1: Quantitative comparison with baselines and ablations on test set of Scannet dataset [8].

Method	Acc ↓	Compl ↓	Chamfer ↓	Prec ↑	Recall ↑	F-score ↑
RevisitingSI [18]	14.29	16.19	15.24	0.346	0.293	0.314
MVDepthNet [42]	12.94	8.34	10.64	0.443	0.487	0.460
GPMVS [17]	12.90	8.02	10.46	0.453	0.510	0.477
ESTDepth [26]	12.71	7.54	10.12	0.456	0.542	0.491
DPSNet [19]	11.94	7.58	9.77	0.474	0.519	0.492
DELTAS [38]	11.95	7.46	9.71	0.478	0.533	0.501
DeepVideoMVS [13]	10.68	**6.90**	8.79	0.541	0.592	0.563
COLMAP [37]	10.22	11.88	11.05	0.509	0.474	0.489
NeuralRecon [39]	**5.09**	9.13	7.11	0.630	**0.612**	0.619
Atlas [18]	7.16	7.61	7.38	0.675	0.605	0.636
Ours: w/o TRSF, avg	7.23	9.74	8.48	0.635	0.501	0.557
Ours: w/o TRSF, pred	6.11	11.12	8.61	0.686	0.512	0.583
Ours: w/o spatial ref.	10.46	16.91	13.68	0.479	0.295	0.361
Ours: 4 images, RND	8.01	10.28	9.15	0.587	0.445	0.502
Ours: 4 images	6.80	8.40	7.60	0.661	0.524	0.581
Ours: 8 images, RND	6.74	8.55	7.64	0.665	0.544	0.596
Ours: 8 images	6.17	7.69	6.93	0.704	0.584	0.636
Ours: 16 images, RND	5.80	8.56	7.18	0.711	0.584	0.638
Ours: w/o C2F filter	6.57	7.69	7.13	0.678	0.592	0.631
Ours	5.52	8.27	**6.89**	**0.728**	0.600	**0.655**

4.1 Comparison with State of the Art

In Tab. 2, we compare our approach with state-of-the-art methods. All methods are trained on the ScanNet dataset [8], using the official train/val/test split. We use the pre-trained models provided by the authors for MVDepthNet [42], GPMVS [17] and DPSNet [19] which are fine-tuned on ScanNet. For baselines that predict depth in a reference camera frame instead of directly reconstructing 3D surface, a volumetric fusion method [6] is used to fuse different depth maps into a 3D truncated signed distance field. The single-view depth prediction method RevisitingSI [18] suffers from the more challenging task formulation without the use of multiple views, leading to noisier depth predictions and inconsistencies between frames. Multi-view depth estimation methods leverage the additional view information for improved performance, with the LSTM-based approach of DeepVideoMVS [13] achieving the best performance among these approaches. Reconstruction quality further improves with methods that directly predict the 3D surface geometry, such as NeuralRecon [39] and Atlas [28]. Our transformer-based feature fusion approach enables more robust reconstruction and outperforms all existing methods in both chamfer distance and F-score. The performance improvement can also be clearly seen in the qualitative comparisons in Fig. 3.

4.2 Ablations

To demonstrate the effectiveness of our design choices, we conducted a quantitative ablation study which is shown in Tab. 2 and discussed in the following.

What is the impact of learning to fuse features from different views with transformers? We evaluate the effect of our learned feature fusion by replacing the transformer blocks with a multi-layer perceptron (MLP) that processes input image observations independently. The per-view outputs of this MLP are fused using an average (*w/o TRSF, avg*) or using a weighted average with weights predicted by the MLP (*w/o TRSF, pred*). We find that our transformer-based view fusion effectively learns to attend to the most informative views for a specific location, resulting in significantly improved performance over these averaging-based feature fusion alternatives.

Does spatial feature refinement help reconstruction performance? Spatial feature refinement is indeed very important for reconstruction quality. It enables the model to aggregate feature information

in spatial domain and produce more spatially consistent and complete reconstructions, without it (*w/o spatial ref.*) the geometry completion (and recall metric) are considerably worse.

How important is coarse-to-fine filtering? Predicting the coarse and fine near-surface masks provides an additional performance improvement compared to the model without it (*w/o C2F filter*), as it allows more focus on surface geometry. Furthermore, this enables a speed-up of the fusion runtime by a factor of approximately 3.5, resulting in processing times of 7 FPS (instead of 2 FPS).

How many views should be used for feature fusion? In our experiments, we use a limited number of $K = 16$ frame observations to inform the feature for every 3D grid location. We find that these views all contribute, with performance degrading somewhat with sparser sets of observations ($K = 8$ or $K = 4$). The number of frames is limited because of execution time and memory consumption for bigger scenes.

How effective is frame selection using attention weights? The K frames for each 3D grid feature are selected based on the computed attention weights and are updated during scanning. To evaluate this frame selection, we compare against a frame selection scheme that randomly selects frames that observe the 3D location (*RND*), which results in a noticeable drop in performance for both chamfer and F-score. The performance difference is even larger when using less views for fusion ($K = 8$ or $K = 4$), where view selection becomes even more important. In Fig. 1, we visualize the most important view for locations in the scene, selected by the highest attention weight. Relatively smooth transitions between selected views among neighboring 3D locations suggest that view selection is spatially consistent. To illustrate the frame selection, we also visualize all selected frames with corresponding attention weights for specific 3D locations in the supplemental document.

4.3 Limitations

Under severe occlusions and partial observation of the scene, our method can struggle to reconstruct details of certain objects, such as chair legs, monitor stands, or books on the shelves. Furthermore, transparent objects, such as glass windows without frames, are often inaccurately reconstructed as empty space. We show qualitative examples of these failure cases in the supplemental material. These challenging scenarios are often not properly reconstructed even when using ground truth RGB-D data, and we believe that using self-supervised losses [10] for monocular scene reconstruction could be an interesting future research direction. Additionally, higher resolution geometric fidelity could potentially be achieved by sparse operations in 3D or learning local geometric priors on detailed synthetic data [21].

5 Conclusion

We introduced TransformerFusion for monocular 3D scene reconstruction, leveraging a new transformer-based approach for online feature fusion from RGB input views. A coarse-to-fine formulation of our transformer-based feature fusion improves the effective reconstruction performance as well as the runtime. Our feature fusion learns to exploit the most informative image view features for geometric reconstruction, achieving state-of-the-art reconstruction performance. We believe that our interactive scanning approach provides exciting avenues for future research, and enables new possibilities in learning multi-view perception and 3D scene understanding.
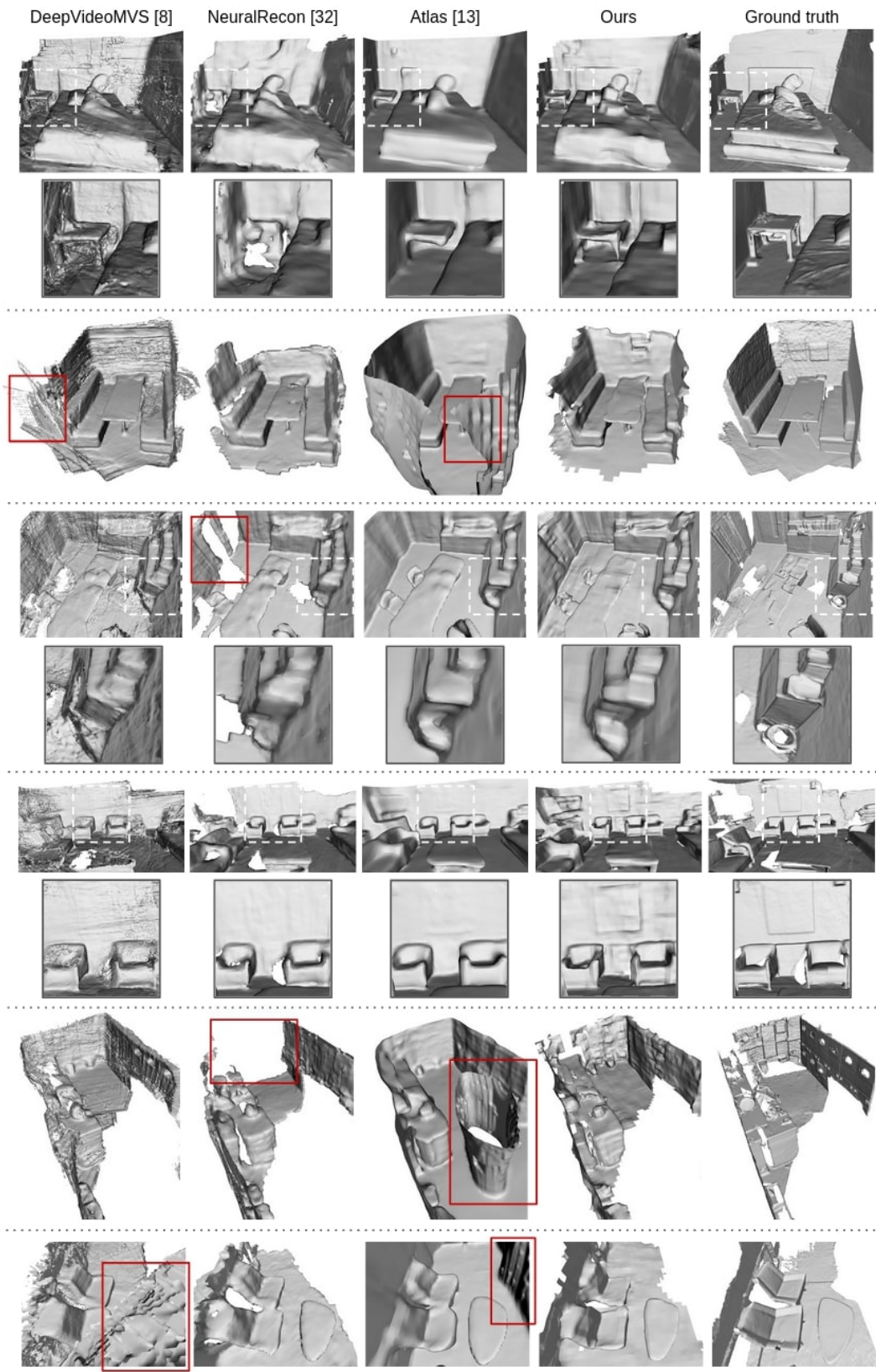
Figure 3: Qualitative comparison of scene reconstructions on test set of ScanNet dataset [8]; note that only RGB input is used by each method while the ground truth is reconstructed using the input depth.

References

[1] M. Bleyer, C. Rhemann, and C. Rother. Patchmatch stereo-stereo matching with slanted support windows. In *Bmvc*, volume 11, pages 1–11, 2011.

[2] T. B. Brown, B. Mann, N. Ryder, M. Subbiah, J. Kaplan, P. Dhariwal, A. Neelakantan, P. Shyam, G. Sastry, A. Askell, et al. Language models are few-shot learners. *arXiv preprint arXiv:2005.14165*, 2020.

[3] C. Campos, R. Elvira, J. J. G. Rodríguez, J. M. Montiel, and J. D. Tardós. Orb-slam3: An accurate open-source library for visual, visual-inertial and multi-map slam. *arXiv preprint arXiv:2007.11898*, 2020.

[4] N. Carion, F. Massa, G. Synnaeve, N. Usunier, A. Kirillov, and S. Zagoruyko. End-to-end object detection with transformers. In *European Conference on Computer Vision*, pages 213–229. Springer, 2020.

[5] J. Chibane, T. Alldieck, and G. Pons-Moll. Implicit functions in feature space for 3d shape reconstruction and completion. In *IEEE Conference on Computer Vision and Pattern Recognition (CVPR)*. IEEE, jun 2020.

[6] B. Curless and M. Levoy. A volumetric method for building complex models from range images. In *Proceedings of the 23rd annual conference on Computer graphics and interactive techniques*, pages 303–312, 1996.

[7] A. Dai and M. Nießner. 3dmv: Joint 3d-multi-view prediction for 3d semantic scene segmentation. In *Proceedings of the European Conference on Computer Vision (ECCV)*, pages 452–468, 2018.

[8] A. Dai, A. X. Chang, M. Savva, M. Halber, T. Funkhouser, and M. Nießner. Scannet: Richly-annotated 3d reconstructions of indoor scenes. In *Proceedings of the IEEE Conference on Computer Vision and Pattern Recognition*, pages 5828–5839, 2017.

[9] A. Dai, M. Nießner, M. Zollhöfer, S. Izadi, and C. Theobalt. Bundlefusion: Real-time globally consistent 3d reconstruction using on-the-fly surface reintegration. *ACM Transactions on Graphics (ToG)*, 36(4):1, 2017.

[10] A. Dai, C. Diller, and M. Nießner. Sg-nn: Sparse generative neural networks for self-supervised scene completion of rgb-d scans. In *Proceedings of the IEEE/CVF Conference on Computer Vision and Pattern Recognition*, pages 849–858, 2020.

[11] J. Devlin, M.-W. Chang, K. Lee, and K. Toutanova. Bert: Pre-training of deep bidirectional transformers for language understanding. *arXiv preprint arXiv:1810.04805*, 2018.

[12] A. Dosovitskiy, L. Beyer, A. Kolesnikov, D. Weissenborn, X. Zhai, T. Unterthiner, M. Dehghani, M. Minderer, G. Heigold, S. Gelly, et al. An image is worth 16x16 words: Transformers for image recognition at scale. *arXiv preprint arXiv:2010.11929*, 2020.

[13] A. Düzçeker, S. Galliani, C. Vogel, P. Speciale, M. Dusmanu, and M. Pollefeys. Deepvideomvs: Multi-view stereo on video with recurrent spatio-temporal fusion, 2020.

[14] K. He, X. Zhang, S. Ren, and J. Sun. Deep residual learning for image recognition. In *Proceedings of the IEEE conference on computer vision and pattern recognition*, pages 770–778, 2016.

[15] J. Hou, A. Dai, and M. Nießner. 3d-sis: 3d semantic instance segmentation of rgb-d scans. In *Proceedings of the IEEE/CVF Conference on Computer Vision and Pattern Recognition*, pages 4421–4430, 2019.

[16] J. Hou, A. Dai, and M. Nießner. Revealnet: Seeing behind objects in rgb-d scans. In *Proceedings of the IEEE/CVF Conference on Computer Vision and Pattern Recognition*, pages 2098–2107, 2020.

[17] Y. Hou, J. Kannala, and A. Solin. Multi-view stereo by temporal nonparametric fusion. In *Proceedings of the IEEE/CVF International Conference on Computer Vision*, pages 2651–2660, 2019.

[18] J. Hu, M. Ozay, Y. Zhang, and T. Okatani. Revisiting single image depth estimation: Toward higher resolution maps with accurate object boundaries. 2019.

[19] S. Im, H.-G. Jeon, S. Lin, and I. S. Kweon. Dpsnet: End-to-end deep plane sweep stereo. *arXiv preprint arXiv:1905.00538*, 2019.

[20] M. Ji, J. Gall, H. Zheng, Y. Liu, and L. Fang. Surfacenet: An end-to-end 3d neural network for multiview stereopsis. In *Proceedings of the IEEE International Conference on Computer Vision*, pages 2307–2315, 2017.

[21] C. Jiang, A. Sud, A. Makadia, J. Huang, M. Nießner, T. Funkhouser, et al. Local implicit grid representations for 3d scenes. In *Proceedings of the IEEE/CVF Conference on Computer Vision and Pattern Recognition*, pages 6001–6010, 2020.

[22] S. Khan, M. Naseer, M. Hayat, S. W. Zamir, F. S. Khan, and M. Shah. Transformers in vision: A survey. *arXiv preprint arXiv:2101.01169*, 2021.

[23] D. P. Kingma and J. Ba. Adam: A method for stochastic optimization. *arXiv preprint arXiv:1412.6980*, 2014.

[24] A. Krizhevsky, I. Sutskever, and G. E. Hinton. Imagenet classification with deep convolutional neural networks. *Advances in neural information processing systems*, 25:1097–1105, 2012.

[25] C. Liu, J. Gu, K. Kim, S. G. Narasimhan, and J. Kautz. Neural rgb (r) d sensing: Depth and uncertainty from a video camera. In *Proceedings of the IEEE/CVF Conference on Computer Vision and Pattern Recognition*, pages 10986–10995, 2019.

[26] X. Long, L. Liu, W. Li, C. Theobalt, and W. Wang. Multi-view depth estimation using epipolar spatio-temporal network. *CVPR*, 2021.

[27] W. E. Lorensen and H. E. Cline. Marching cubes: A high resolution 3d surface construction algorithm. *ACM siggraph computer graphics*, 21(4):163–169, 1987.

[28] Z. Murez, T. van As, J. Bartolozzi, A. Sinha, V. Badrinarayanan, and A. Rabinovich. Atlas: End-to-end 3d scene reconstruction from posed images. In *ECCV*, 2020. URL `https://arxiv.org/abs/2003.10432`.

[29] Y. Nie, J. Hou, X. Han, and M. Nießner. Rfd-net: Point scene understanding by semantic instance reconstruction. *arXiv preprint arXiv:2011.14744*, 2020.

[30] N. Parmar, A. Vaswani, J. Uszkoreit, L. Kaiser, N. Shazeer, A. Ku, and D. Tran. Image transformer. In *International Conference on Machine Learning*, pages 4055–4064. PMLR, 2018.

[31] A. Paszke, S. Gross, F. Massa, A. Lerer, J. Bradbury, G. Chanan, T. Killeen, Z. Lin, N. Gimelshein, L. Antiga, et al. Pytorch: An imperative style, high-performance deep learning library. *arXiv preprint arXiv:1912.01703*, 2019.

[32] S. Peng, M. Niemeyer, L. Mescheder, M. Pollefeys, and A. Geiger. Convolutional occupancy networks. In *European Conference on Computer Vision (ECCV)*, Cham, Aug. 2020. Springer International Publishing.

[33] V. Pradeep, C. Rhemann, S. Izadi, C. Zach, M. Bleyer, and S. Bathiche. Monofusion: Real-time 3d reconstruction of small scenes with a single web camera. In *2013 IEEE International Symposium on Mixed and Augmented Reality (ISMAR)*, pages 83–88. IEEE, 2013.

[34] C. R. Qi, H. Su, K. Mo, and L. J. Guibas. Pointnet: Deep learning on point sets for 3d classification and segmentation. In *Proceedings of the IEEE conference on computer vision and pattern recognition*, pages 652–660, 2017.

[35] C. R. Qi, L. Yi, H. Su, and L. J. Guibas. Pointnet++: Deep hierarchical feature learning on point sets in a metric space. *arXiv preprint arXiv:1706.02413*, 2017.

[36] C. R. Qi, O. Litany, K. He, and L. J. Guibas. Deep hough voting for 3d object detection in point clouds. In *Proceedings of the IEEE/CVF International Conference on Computer Vision*, pages 9277–9286, 2019.

[37] J. L. Schönberger, E. Zheng, M. Pollefeys, and J.-M. Frahm. Pixelwise View Selection for Unstructured Multi-View Stereo. In *European Conference on Computer Vision (ECCV)*, 2016.

[38] A. Sinha, Z. Murez, J. Bartolozzi, V. Badrinarayanan, and A. Rabinovich. Deltas: Depth estimation by learning triangulation and densification of sparse points. In *ECCV*, 2020. URL `https://arxiv.org/abs/2003.08933`.

[39] J. Sun, Y. Xie, L. Chen, X. Zhou, and H. Bao. NeuralRecon: Real-time coherent 3D reconstruction from monocular video. *CVPR*, 2021.

[40] A. Vaswani, N. Shazeer, N. Parmar, J. Uszkoreit, L. Jones, A. N. Gomez, L. Kaiser, and I. Polosukhin. Attention is all you need. *arXiv preprint arXiv:1706.03762*, 2017.

[41] L. von Stumberg, V. Usenko, and D. Cremers. Direct sparse visual-inertial odometry using dynamic marginalization. In *International Conference on Robotics and Automation (ICRA)*, May 2018.

[42] K. Wang and S. Shen. Mvdepthnet: Real-time multiview depth estimation neural network. In *2018 International conference on 3d vision (3DV)*, pages 248–257. IEEE, 2018.

[43] W. Wang, R. Yu, Q. Huang, and U. Neumann. Sgpn: Similarity group proposal network for 3d point cloud instance segmentation. In *Proceedings of the IEEE Conference on Computer Vision and Pattern Recognition*, pages 2569–2578, 2018.

[44] X. Wang, R. Girshick, A. Gupta, and K. He. Non-local neural networks. In *Proceedings of the IEEE conference on computer vision and pattern recognition*, pages 7794–7803, 2018.

[45] P. Zins, Y. Xu, E. Boyer, S. Wuhrer, and T. Tung. Learning implicit 3d representations of dressed humans from sparse views. *arXiv preprint arXiv:2104.08013*, 2021.
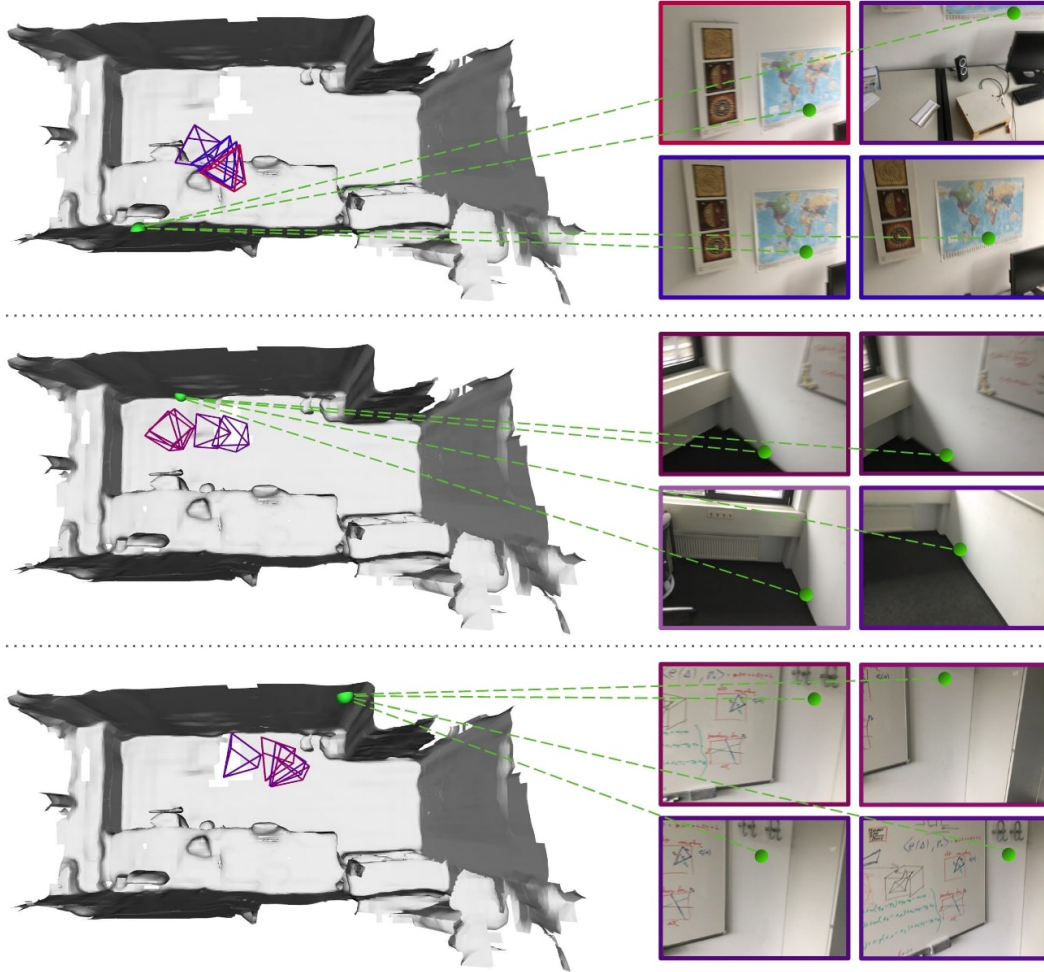
Figure 4: Visualization of selected camera views with self-supervised attention weights (lower weights are visualized as *blue* and higher as *red*) for specific 3D locations (highlighted as *green*) in the scene.

A Additional Results

Visualization of Frame Selection. In Fig. 4, we show a 3D reconstruction of a scene from the test set of the ScanNet dataset [8]. To visualize the view selection approach presented in the main paper that is based on the attention weights of the used transformer networks, we render the camera views that are selected for a specific 3D location (green point) with corresponding attention weights (color temperature corresponding to the weight). On the right, we show the corresponding input images.

Additional Ablation Studies. As analyzed in the main document, the different algorithmic parts of our methods play an important role. Fig. 5 shows qualitative results for the ablation study. Specifically, one can clearly see the impact of the spatial refinement as well as the temporal feature fusion via our transformer architecture. For qualitative results of the setting without using transformers for feature fusion we use predicted weights for weighted averaging of features via an MLP.

In Tab. 2, we conducted an additional quantitative ablation study w.r.t. the input to the transformer networks. As can be seen, both the projected depth as well as the view ray help the transformer to better fuse the features for the task of 3D reconstruction.

In Fig. 6, we show a comparison of our view selection scheme to the baseline that takes random views from the view candidates (views that contain a specific point). Specifically, we vary the number
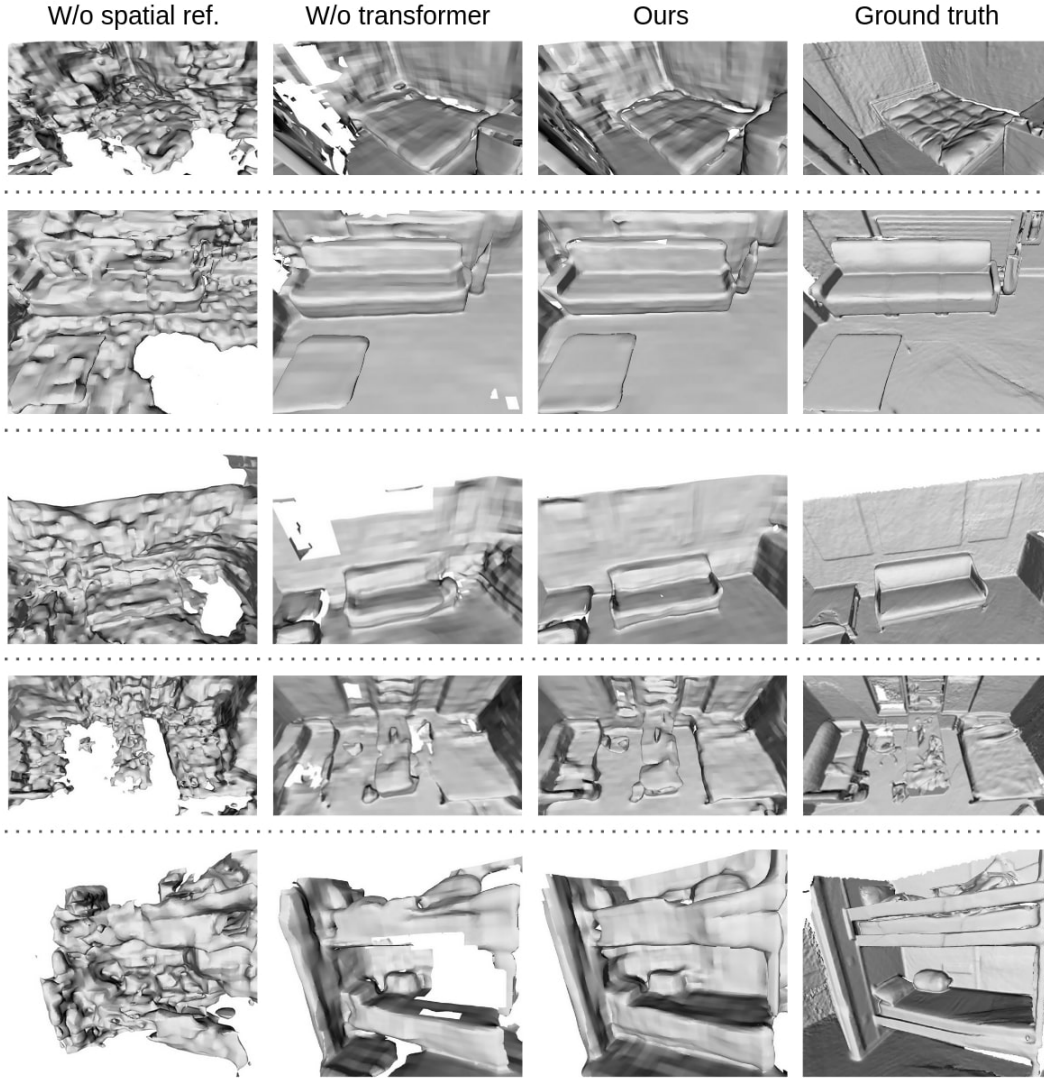
Figure 5: Qualitative comparison of ablations of our approach on test set of ScanNet dataset [8]; note that only RGB input is used by each method while the ground truth is reconstructed using the input depth.

of views that can be selected. As can be seen, the reconstruction quality gap between the baseline and our method increases with less views which is to be expected since the random selection is more likely to miss important views.

Table 2: Quantitative ablation study on the transformer inputs, conducted on the test set of the ScanNet dataset [8].

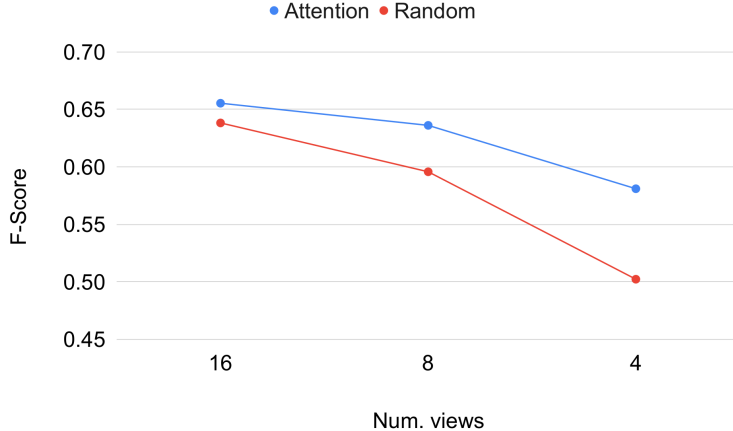| Method	Acc $\downarrow$	Compl $\downarrow$	Chamfer $\downarrow$	Prec $\uparrow$	Recall $\uparrow$	F-score $\uparrow$
Ours: w/o projected depth	8.06	10.02	9.04	0.594	0.475	0.525
Ours: w/o view ray	5.71	8.59	7.15	0.706	0.559	0.621
Ours	**5.52**	**8.27**	**6.89**	**0.728**	**0.600**	**0.655**

13

Figure 6: Comparison of our attention-based view selection scheme to a random selection of frames from the frame candidates based on the F-score.

Additional Qualitative Results. In Fig. 11 further examples are shown that demonstrate the reconstruction capability of our approach. We show a top down, as well as a view from inside the different reconstructed room scenes.

B   Reproducibility

Table 3: Runtime analysis of our per-frame feature fusion.

Task	Duration
Image loading / feature extraction	21.50ms
Coarse feature fusion	11.81ms
Near-surface mask prediction	24.18ms
Fine feature fusion	73.03ms
Total	130.52ms

Table 4: Runtime analysis of the per-chunk mesh extraction.

Task	Duration
Coarse feature refinement	28.56ms
Fine feature refinement	140.79ms
MLP (occupancy prediction)	25.21ms
Marching cubes [27]	48.74ms
Total	243.29ms

Runtime Analysis. In this section we provide further details about the runtime of our approach. We benchmarked our approach using an Intel Xeon 6242R Processor and an Nvidia RTX 3090 GPU. For every new frame coarse-to-fine image features need to be extracted, and fused into global coarse and fine feature volumes. In Tab. 3, we report execution times of the different feature fusion steps. Coarse features are fused into the entire camera frustum, containing all coarse voxels that fall into valid depth range $[0.3\mathrm{m}, 5\mathrm{m}]$. Fine feature on the other hand are fused only in near-surface areas, as predicted by coarse filtering. The execution times are averaged over a representative video sequence of the ScanNet dataset. Note that surface reconstruction doesn't need to be extracted for every frame. It can either be done at the end, when all image features are already fused into the feature volume, or incrementally every couple of frames, on a per-chunk basis, if interactive feedback is desired. In Tab. 4, we report execution times for a chunk of size $1.5 \times 1.5 \times 1.5$ m. Both, coarse and fine features are spatially refined using a 3D CNN and surface occupancy is computed using the occupancy MLP at a voxel resolution of 2 cm, but only for near-surface voxels, as predicted by coarse and fine near-surface masks. Finally, the mesh is extracted using Marching cubes [27]. Note that our implementation uses high-level PyTorch routines, as well as CPU code (e.g., for Marching Cubes) and, thus, the implementation is not optimized for runtime. A more optimized implementation can be achieved via customized CUDA code. Another interesting avenue towards higher frame rates is the use of sparse 3D convolutions instead of dense 3D convolutions. Feature fusion timings are reported for our default reconstruction setting, when we store $K = 16$ views for every feature grid voxel. The feature fusion execution can be further accelerated by using less views. The frames per second (FPS) increase from 7.66 FPS for 16 views to 10.17 FPS for 8 and to 12.28 FPS for 4 views.

14

Network Architectures.   In Fig. 7, we depict the architectures of the neural networks used in our approach. For both, the coarse and fine layer, we use independent feature fusion and feature refinement networks. The building blocks used in these networks are detailed in Fig. 8.
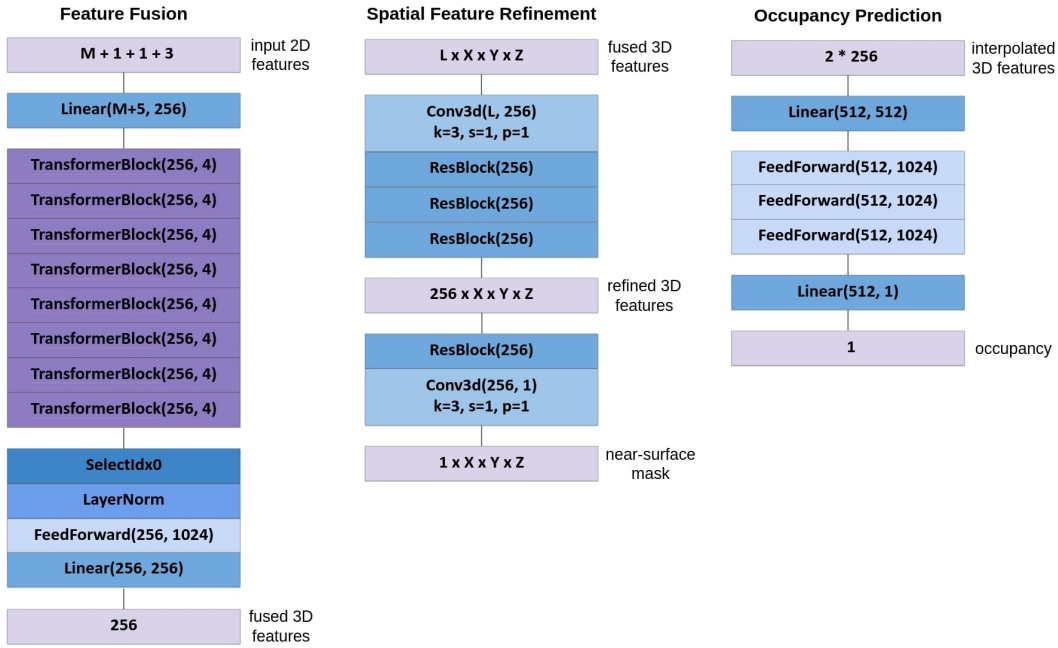

Figure 7: Overview of the used neural networks. Note that we are using a feature fusion and feature refinement network per level (coarse and fine).
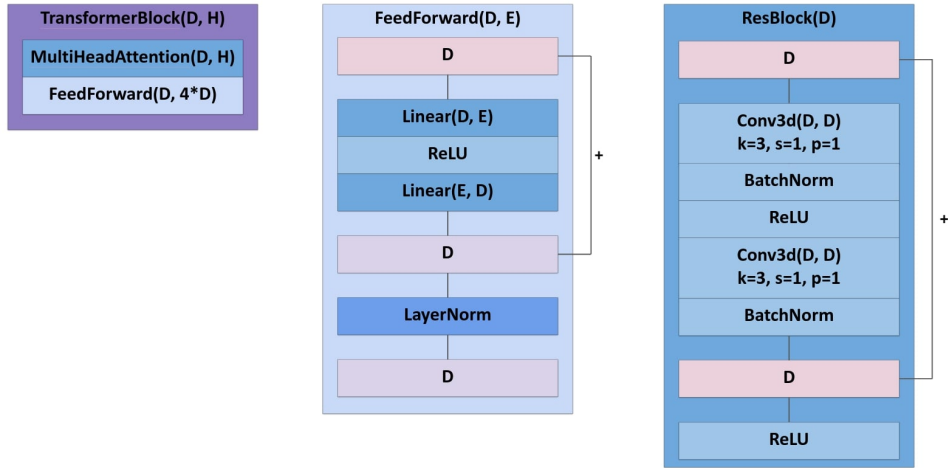

Figure 8: Low-level network details of the building blocks of our pipeline (see Fig. 7).

Reproducibility of Experiments.   To ensure the reproducibility of our experiments, we ran our approach and ablations 3 times. The resulting F-score mean and standard deviation for different experiments is shown is Fig. 9, with standard deviations visualized as error bars.
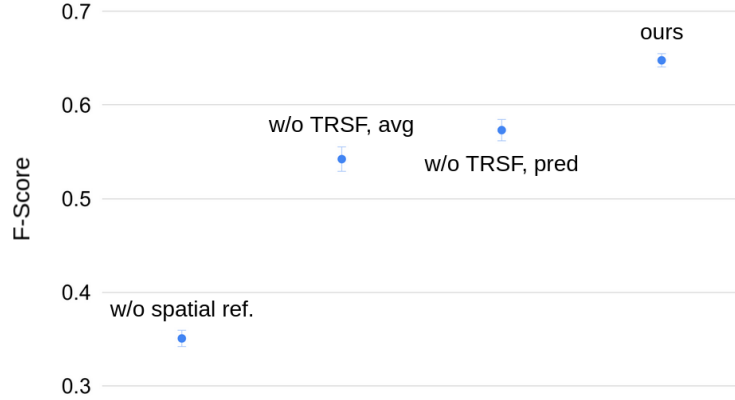
Figure 9: The F-score mean and standard deviation of multiple experiments of our approach and ablations.

C Limitations

In Fig. 10, we present some limitations of our approach. When objects are only partially observed, with a large occluded region, the occluded parts can be missing or lack detail. Examples are missing chair legs, or inaccurate reconstruction of small details such as books. Another challenging scenario for our method is reconstruction of transparent objects, such as glass windows. Most of the time these transparent surfaces get labeled as free-space instead.
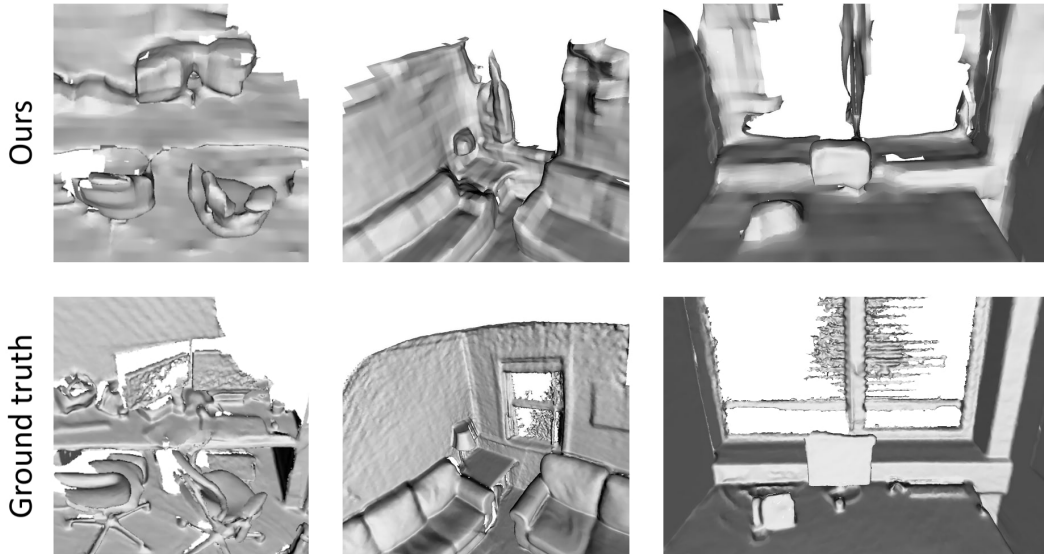

Figure 10: Limitations of our approach are the lack of detail at partially observed and occluded objects, and inaccurate reconstruction of transparent surfaces, such as glass windows.

D Data

To train and evaluate our method, we use the ScanNet dataset [8], which is available under a non-commercial academic license[1]. ScanNet collects data of static indoor environments, and the ScanNet authors report that consent was obtained from the people whose private spaces were scanned. The ScanNet scenes and locations have been anonymized.

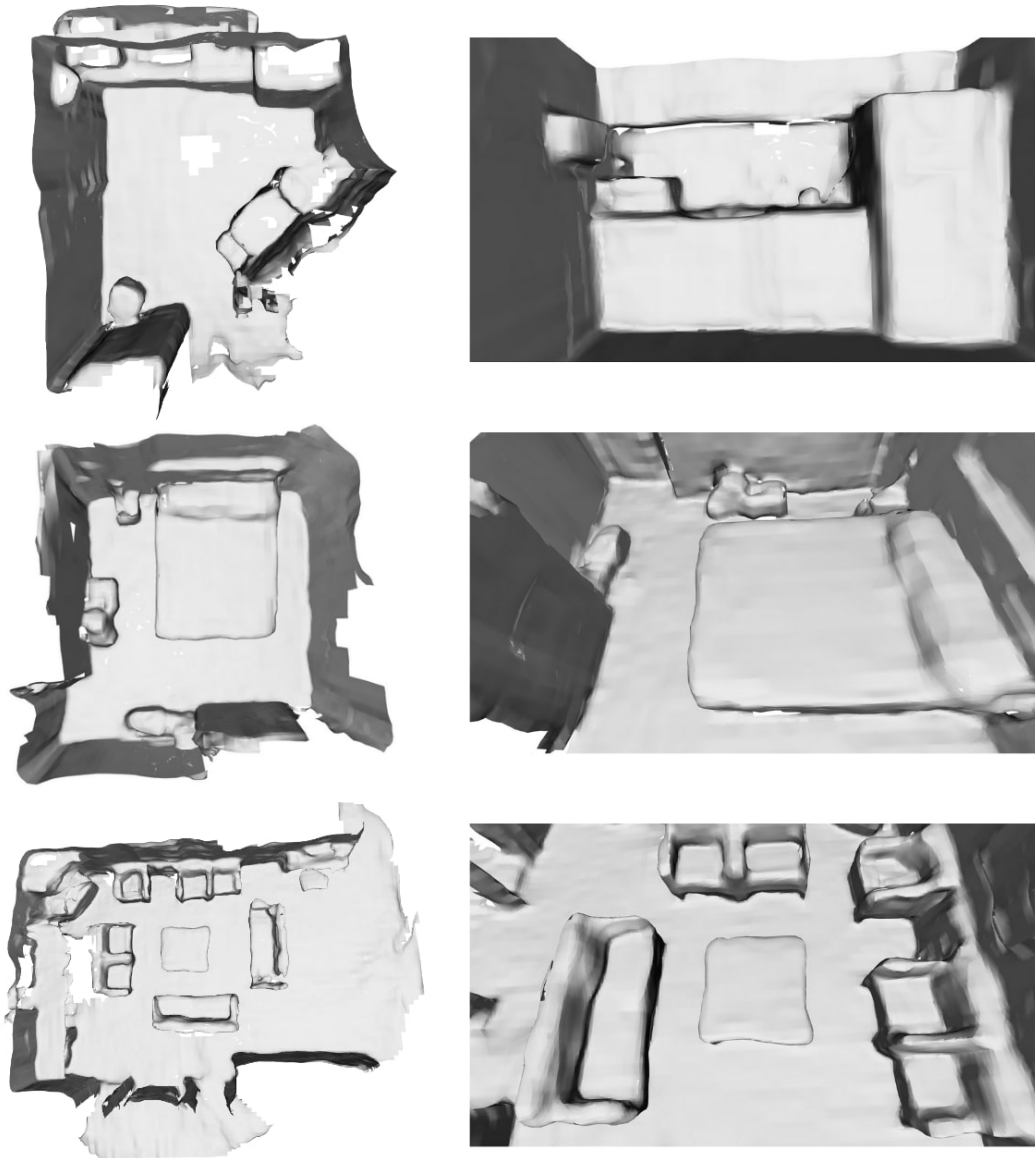[1] http://kaldir.vc.in.tum.de/scannet/ScanNet_TOS.pdf

Figure 11: Qualitative results of representative scenes from the test-set of the ScanNet dataset [8].